

EXPERIMENTAL STUDY OF THE AERODYNAMIC LOADS ON THE AIRFRAME OF A MULTIROTOR UAV

D. Barcelos, A. Haleem and G. Bramesfeld

Ryerson University, Toronto, ON

65th Aeronautics Conference, CASI AERO 21

Abstract

In this study, a wind tunnel experiment was conducted on a multirotor unmanned aerial vehicle airframe in different configurations to help create an experimental database of the aerodynamic loads on the different vehicle components. The experimental database can help validate aerodynamic load prediction approaches to these complex shapes and help identify if using a load build-up approach is feasible. The aerodynamic airframe loads on a multirotor vehicle in forward flight operations can significantly contribute to the overall vehicle loads, and thus a better understanding of the airframe loads can help with the flight predictions of these vehicles. A 1:1 scale model was created based on a modified geometry of the DJI Matrice 210 RTK without rotors. The test model was modular to allow each of the main components to be tested individually. The model was placed in a low-speed wind tunnel and tested for different pitch angles and roll angles to simulate different flight configurations. The lift and drag forces were measured using an external load balance, and the vehicle's orientation was measured using a set of IMUs. Corrections for base loads, blockage effects and buoyancy effects were applied, showing that base loads have the most significant impact and buoyancy corrections had minimal effect. The results showed the lift and drag contribution of each of the main components, including the main body, primary batteries, landing gear, arms/motors, RTK antennas and additional accessories at varying roll and pitch angles. Additionally, a drag build-up had a similar average drag to those measured during the full vehicle test, however, there are notable discrepancies in the trends of these results.

1 Introduction

Experimental testing of the aerodynamic properties of multirotor unmanned aerial vehicles (UAVs) is critical to improving the flight of these vehicles. Typically, the rotor performance is the main focus when considering the overall aerodynamic loads of multirotor UAVs. Controlled wind tunnel testing of multirotor UAVs has largely been on isolated rotor testing such as Refs. 1, 2, 3 & 4 or full vehicle tests such as Refs. 5, 6, 7 & 8. Few studies focus on the airframe loads of these multirotor UAVs, which in forward flight, can significantly contribute to the overall vehicle loads.

Figure 1 is used to help illustrate the magnitude of the airframe forces and moments relative to the overall loads. The figure is based on a one-minute sample of flight test data of a DJI Matrice 210 RTK in which the vehicle was undergoing straight passes back and forth. The rotor loads are predicted using a BEMT approach presented by Carroll et al. [9] and the vehicle body loads are predicted using a simple load build-up approach presented by Tsaltas et al. [10] based on the flight test data. It should be noted that the airframe load build-up approach tends to under-predict the airframe drag, and the interference effects between rotors or the airframe are not modelled. The predicted airframe loads are over 10% of the overall vehicle loads during the forward flight segments. Although Fig. 1 is based on predictions, this clearly illustrates that the airframe loads must be considered when discussing the aerodynamic loads in forward flight.

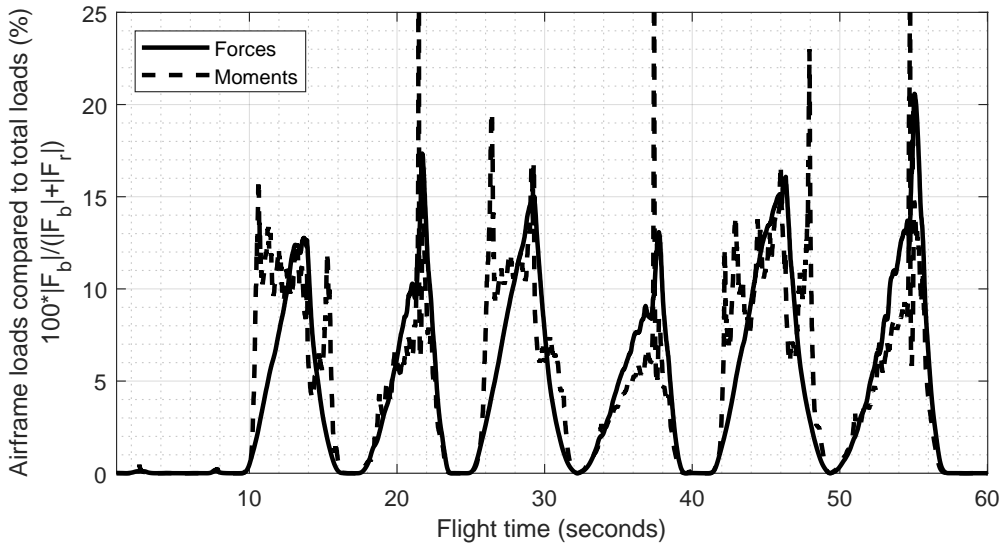


Figure 1: Predicted airframe forces and moments compared to the overall vehicle loads based on DJI Matrice 210 RTK flight test data.

The presented study is an experimental investigation into the airframe loads of a typical multirotor UAV. Seven configurations were tested that include the different airframe components to help better understand the effect of the individual components on the overall vehicle loads. This study describes the experimental setup, including the wind tunnel parameters, the experimental model,

and the different configurations of interest. The testing methodology is described, including the sensors used in this study and the testing procedure. The corrections used are described, which include baseload corrections, blockage effects and buoyancy corrections. The experimental results included the lift and the drag loads on the airframe at different pitch and roll angles. These results aim to provide a database for prediction tools to compare and provide insight into how each typical airframe component attributes to the overall vehicle loads.

2 Experimental Setup

The airframe of the commercially available DJI Matrice 210 RTK was modelled and tested to determine the airframe loads under different flight conditions. The DJI Matrice 210 RTK is a quadcopter UAV with four 17inch diameter rotors, a camera payload and a real-time kinematic (RTK) positioning system. The Matrice was chosen for this study because it consists of components typical of a multirotor UAV, and the vehicle was available for geometric measurements necessary to manufacture the experimental model.

A 1:1 scale model of the Matrice was manufactured out of 3D printed plastic parts, hardwood and carbon fibre depending on the complexity and required strength of each component. Figure 2 shows the fully assembled test model with a description of the nine main components. The main components were modular such that the components could be removed based on the testing methodology. For example, tests were run with and without the camera to identify the airframe loads of the camera system. The components of interest for this study included the main body, main battery below the main body, the landing gear, which includes the legs and feet, the arms, which included the motors, the camera system including the gimbal and the RTK GPS with the mounting arms. Additionally, a few accessories were mounted on the landing gear for research purposes, including a backup battery, computer and secondary antenna.

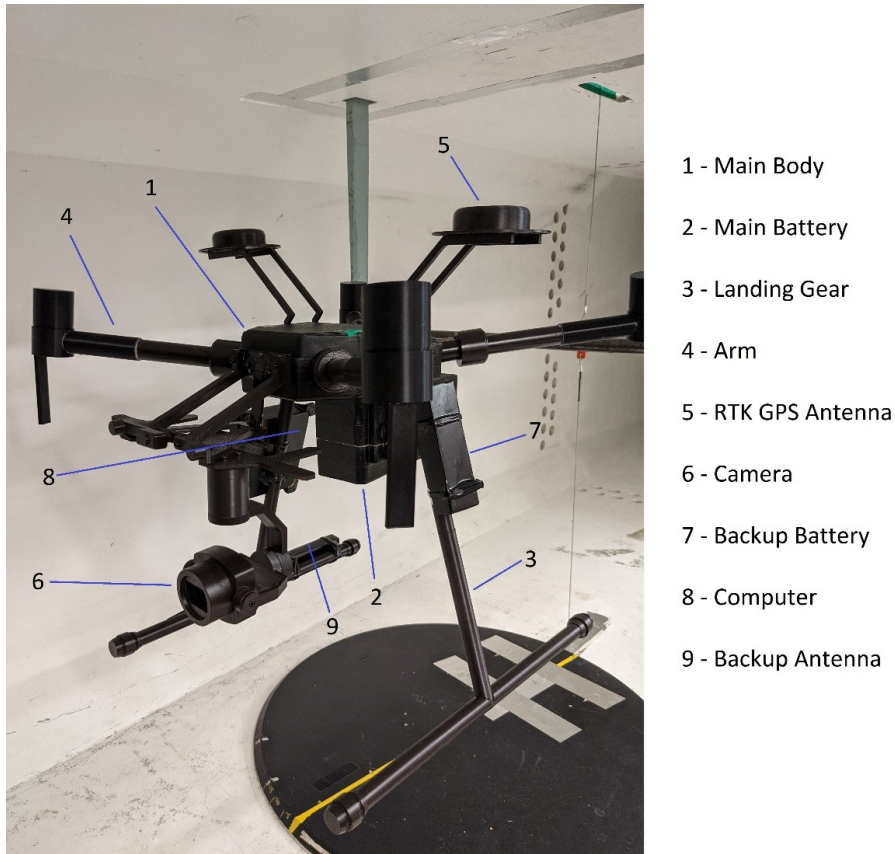


Figure 2: To-scale test model of the DJI Matrice 210 RTK.

The test model was mounted in the Ryerson University low-speed wind tunnel test section. Figure 3 shows the mounting of the Matrice model in the wind tunnel test section. The model was mounted on a metal t-support which is connected to two support struts. The t-support was used because it moves the model ahead of the support struts to help minimize the interference between the model and struts. The t-support was also attached to a pitch-wire which could be raised and lowered to change the model's angle, with the pivot being at the attachment point between the t-support and struts. The pitch-wire could rotate the model from $+35^\circ$ to -40° (where positive is pitch up) and was controlled manually by a knob above the wind tunnel test section. The test model could be mounted at several different roll, pitch and yaw angles to measure the loads at additional angles.

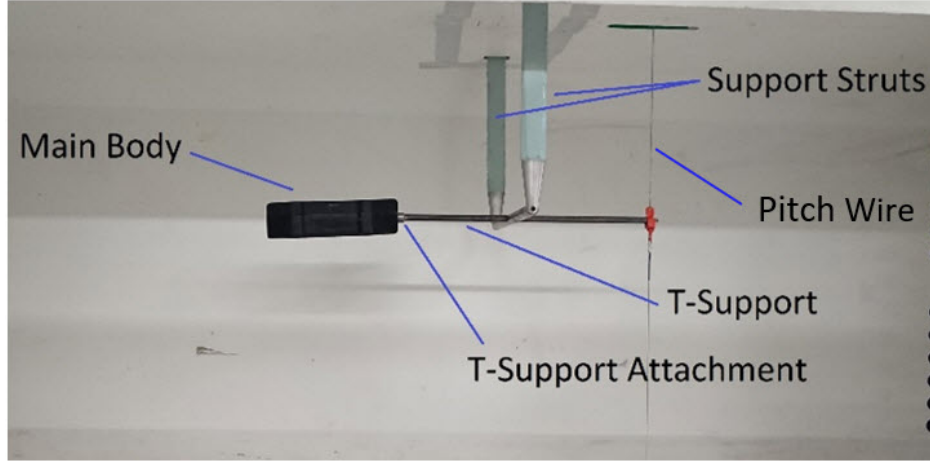


Figure 3: Model mounting in the wind tunnel test section.

The Ryerson University low-speed wind tunnel is a closed-circuit wind tunnel. The test section has a 0.9m x 0.9m cross-section and is approximately 2.75m in length with 45^{circ} corner fillets. The contraction ratio ahead of the test section is 3.2. Turbulence in the tunnel is lowered using turning vanes around each corner and a series of screens directly ahead of the contraction section. The turbulence intensities at the speeds of interest for this study were measured between 0.24% and 0.29% using hot-wire anemometry at the test section center at Kolaei et al. [3]. The wind tunnel is powered by a 200hp electric motor spinning a 1.23m diameter fan. The airspeed is controlled by adjusting the wind tunnel fan rotational speed.

The wind tunnel airspeed, test-section temperature, atmospheric pressure, model loads and vehicle orientation were measured. An Omega PX277 differential pressure transducer was used to measure the dynamic pressure across the nozzle ahead of the test section using the average of 3 static pressure ports around the cross-section of two streamwise locations. The test section temperature was measured using a LabJack EI-1034 temperature probe, and the atmospheric pressure was measured using a Validyne P55A pressure transducer. The loads were measured using a custom TEM force balance above the test section that read the lift and drag forces applied to the support struts. The vehicle orientation was measured using MPU-6050 IMUs connected to an Arduino Uno mounted inside the Matrice model. The Arduino Uno board wirelessly sent the vehicle's orientation to the computer using XBee radios. Except for the vehicle orientation measurements, all sensor measurements were connected to a LabJack T7 data acquisition system (DAQ). Values were read and recorded from the LabJack T7 DAQ and XBee receiver in MATLAB on a desktop computer.

3 Testing Methodology

Before mounting the wind tunnel model, the airspeed and load balance sensors were calibrated. Then the struts and t-support were mounted to measure the base loads. After calibrations were complete, the Matrice model was tested at two airspeeds in seven different configurations of com-

ponents for a sweep of pitch angles and roll angles. Additionally, repeat tests were completed to quantify the reliability of the experimental results. The results were then post-process with suitable corrections.

A pitot-static tube was mounted in the empty test section to calibrate the airspeed sensor at a range of wind tunnel speeds. There was a waiting period of 30 seconds at each wind tunnel fan speed to help the flow stabilize to a constant speed. After the waiting period, the voltage measured by the pressure traducer and the dynamic pressure measured by the pitot-static tube was recorded before moving to the next wind tunnel speed. A linear fit was applied to these results to determine the calibration coefficients. Similarly, the load balance was calibrated before beginning the experiments. The loads were tared, then known lift or drag calibration weights were applied in increment of 100g intervals up to 2kg. The voltage of the lift and drag sensors were also linear fit to the applied loads to determine the calibration equations. Both the airspeed and load balance calibrations were run multiple times to ensure their reliability.

The testing procedure included testing seven different airframe configurations to help understand the loads due to each component. Figure 4 shows a side view of the different configurations tested. The main battery was included in configurations b-g as these configurations were mounted about the main battery.

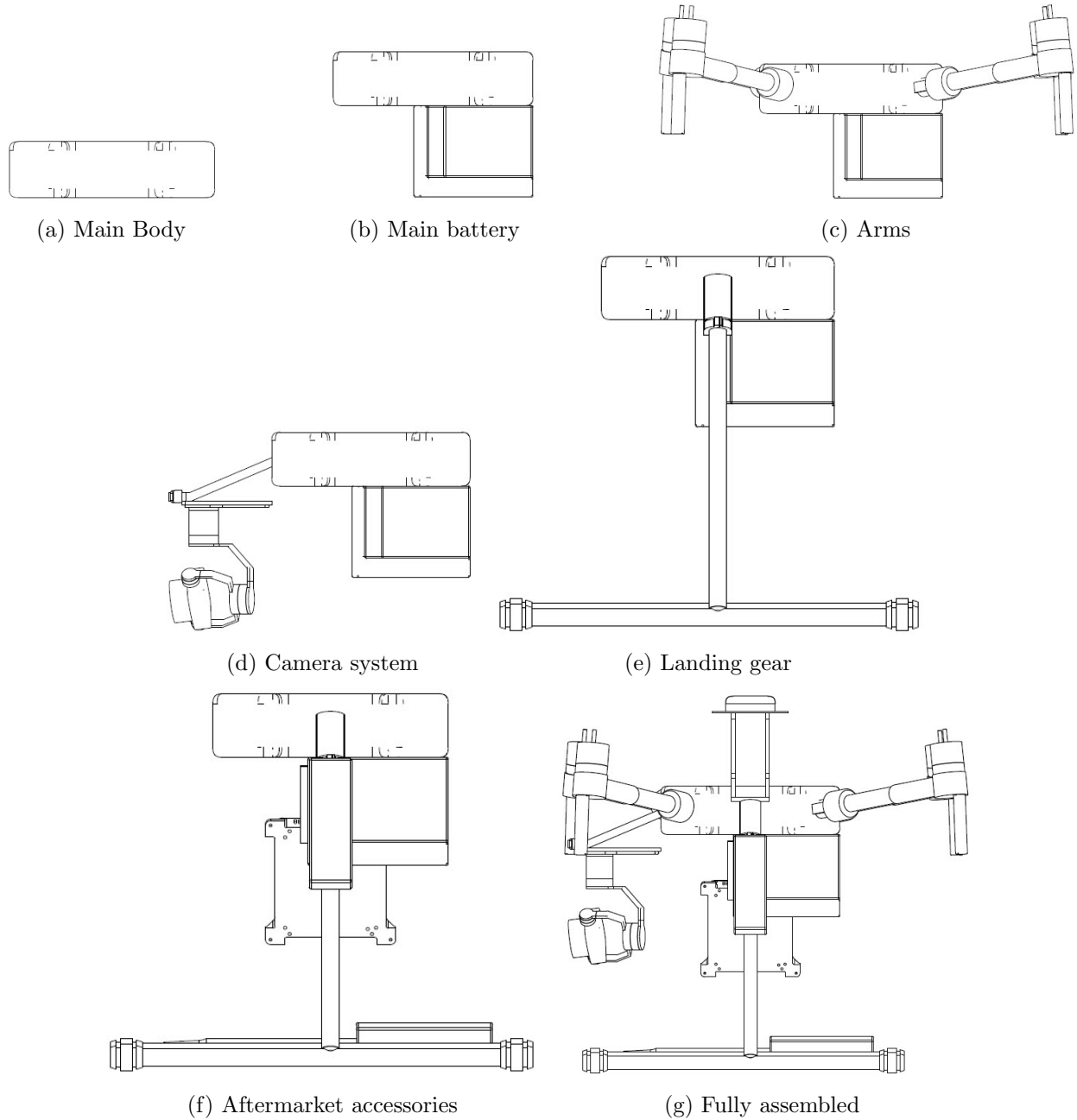


Figure 4: Side view of the seven different airframe configurations tested.

For each of the configurations above, tests were run at 10m/s and 15m/s, however, the results focus on the 15m/s tests. For each configuration, data was collected for a pitch sweep and roll sweep between -135° to 135° in approximately 5° intervals. For each data point, the MATLAB program would wait 30 seconds to allow the flow to settle, then measured one value at a time to avoid cross-talk issues. All data was recorded at 1000hz, beginning with the temperature measurement for 0.5 seconds. Then the tunnel velocity was recorded for 3 seconds, followed by the lift, then drag forces for 3 seconds each. The tunnel velocity and temperature values were then re-recorded to ensure that the flow conditions had not changed while recording the load data. All data is

time-averaged across the reading interval, and the temperature and velocity values are averaged over the two recording periods.

4 Corrections

Corrections were done on the final data sets to help minimize experimental error. The base loads of the struts and t-support used to mount the model were subtracted from the final dataset. Solid and wake blockage corrections were applied to account for the obstruction in airflow due to the reduced available area in the test section. Additionally, a buoyancy correction was applied to account for the boundary layer growth along the wind tunnel's test section walls. From these corrections, the base loads had the most significant impact and whereas the blockage and buoyancy corrections have a minor effect on the final loads.

Base loads

Before mounting the wind tunnel model, baseload measurements were taken to be later used in corrections. The t-support and the struts were mounted in the wind tunnel (with no Matrice model). A tare was complete, and then the wind tunnel was turned on to approximately 3.2m/s. At this speed, the t-support was pitched from -40° to $+35^\circ$ in 5° intervals, recording loads and flow properties at each angle. This pitch sweep was complete for nine wind tunnel speeds from approximately 3m/s to 24m/s. The base loads are converted to coefficient values using a reference area of 1. Each data point collected with the Matrice model then had the base loads subtracted from it by interpolating by the t-support angle and freestream velocity.

Figures 5 & 6 show the non-dimensionalize base loads at varying pitch angles and freestream velocities. As expected, the lift coefficients increase with pitch angle, and the lift is zero at zero pitch angle. The baseload drag coefficients shown in Fig. 6 have a minimum drag at 0 pitch and increase with either positive or negative pitch. Both the lift and drag coefficients have minor changes with respect to velocity, where the differences are due to Reynolds number effects.

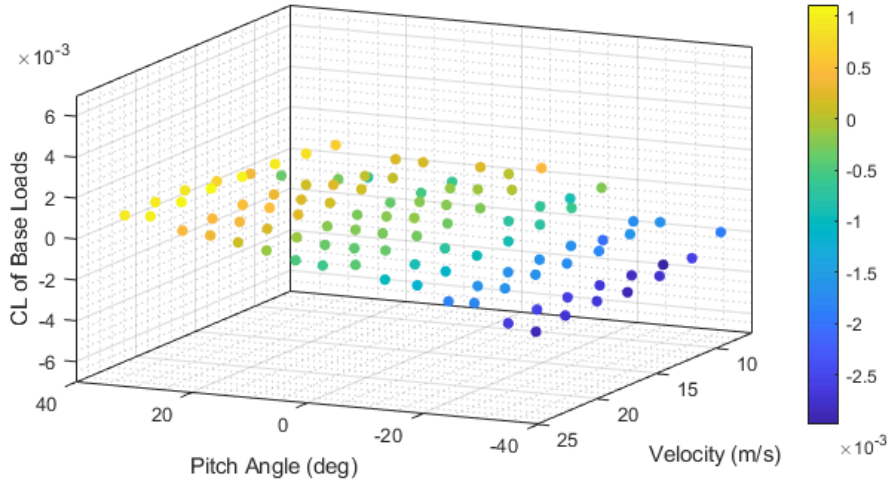


Figure 5: Lift coefficient of base loads at varying angles and freestream velocities.

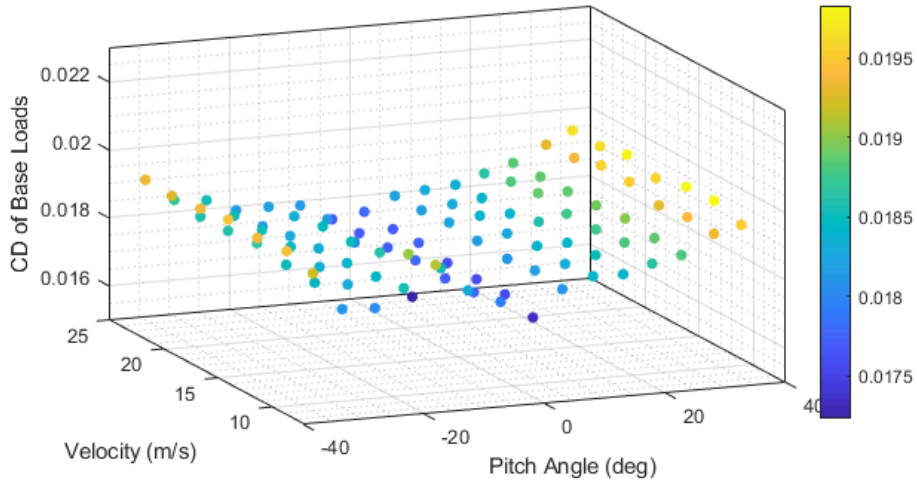


Figure 6: Drag coefficient of base loads at varying angles and freestream velocities.

Blockage Effects

The blockage effects were calculated as solid blockage, and wake blockage corrections based on Barlow et al. [11]. The blockage corrections help account for the reduced effective cross-sectional area in the test section when the model is present. The blockage corrections are used to calculate a corrected dynamic pressure used to non-dimensionalize the measured force values. The solid blockage, ϵ_{SB} can be calculated as:

$$\epsilon_{SB} = \frac{K(V)}{A_{TS}^{3/2}} \quad (1)$$

where K is the body shape factor which is a constant 0.96 for blunt bodies, V is the volume of the model and A_{TS} is the cross-sectional area of the wind tunnel test section. The wake blockage

correction, ϵ_{WB} , can be calculated as:

$$\epsilon_{WB} = \frac{A_M}{4A_C S} C_{Du} \quad (2)$$

where A_M is the frontal area of the model and C_{Du} is the uncorrected drag coefficient. The corrected dynamic pressure, q_c , due to blockage effects is calculated as:

$$q_c = q_u [1 + (\epsilon_{SB} + \epsilon_{WB})]^2 \quad (3)$$

where q_u is the uncorrected dynamic pressure. These new corrected dynamic pressure can then be used to non-dimensionalize the uncorrected force values.

Table 1 shows the blockage correction for each model configuration. The values are the percent difference in dynamic pressure on the model due to the blockage effects. The range for each configuration shows the minimum and maximum changes, which vary due to the different wind tunnel velocities and the front areas at different angles. The blockage corrections become more evident with the larger configurations, as expected.

Table 1: Blockage correction for each configurations

Configuration As Per Fig. 4	Percent Difference in Dynamic Pressure
a) Main Body	0.556% to 0.597%
b) Main Battery	0.546% to 0.629%
c) Arms	1.276% to 1.390%
d) Camera	1.110% to 1.260%
e) Landing gear	1.237% to 1.345%
f) Aftermarket accessories	1.529% to 2.122%
g) Fully assembled	2.058% to 2.874%

Buoyancy Corrections

Buoyancy corrections were used to account for the variation in static pressure along the wind tunnel test section without a model present. The effective cross-sectional area of the test section is consequently smaller due to the boundary layers along the wall. The buoyancy corrections are based on those presented by Barlow et al. [11]. The effective test section cross-sectional area, $A_{effective}$, is calculated as:

$$A_{effective} = A_{TS} - 2[\delta^*(W + H) - 2(\delta^*)^2] \quad (4)$$

where W is the test section width, H is the test section height and δ^* is the displacement thickness of the boundary layer. For a laminar boundary layer, the displacement thickness can be assumed to be:

$$\delta^* = \frac{1.72x}{\sqrt{Re_x}} \quad (5)$$

where x is the test section length and Re_x is the Reynolds number along the length, x . The static pressure change due to the change in test section area by the growth of the boundary layer is calculated as:

$$P = \frac{1}{2}\rho\left(\frac{A_{TS}}{A_{effective}}V_1\right)\left(1 - \frac{A_{effective}}{A_{TS}}\right)^2 \quad (6)$$

where ρ is the freestream density and V_1 is the measured test section velocity. The corrected additional buoyancy drag force, D_B , can be calculated as a function of test section location, x :

$$D_B = \frac{dP}{dx} \times \frac{dA_{effective}}{dx} \quad (7)$$

Figure 7 shows the buoyancy corrected drag coefficient for each of the data points collected in this study (represented by the coloured lines). It should be noted that the drag force was non-dimensionalized using a reference area of 1. The black solid and dashed lines represented the x-locations occupied by the fully assembled Matrice model. The buoyancy effects are nearly negligible as the buoyancy drag coefficients are less than 0.16% of the drag values recorded in the experiments.

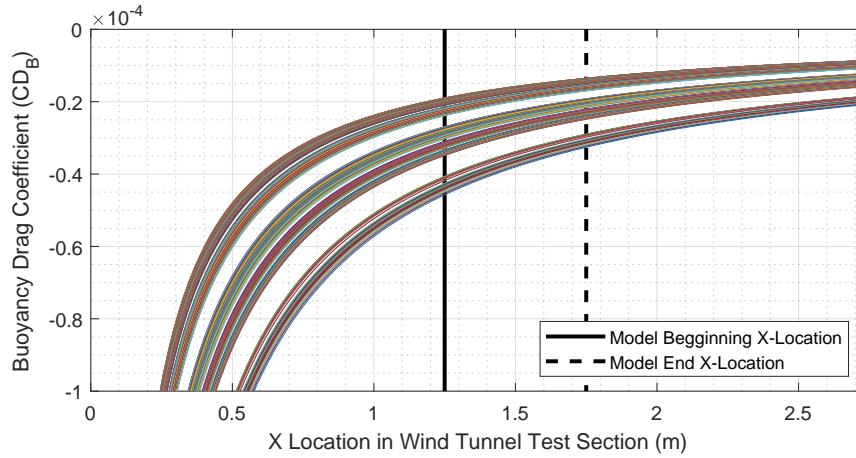


Figure 7: Buoyancy corrections along the length of the test section, different lines represent all of the different data points collected.

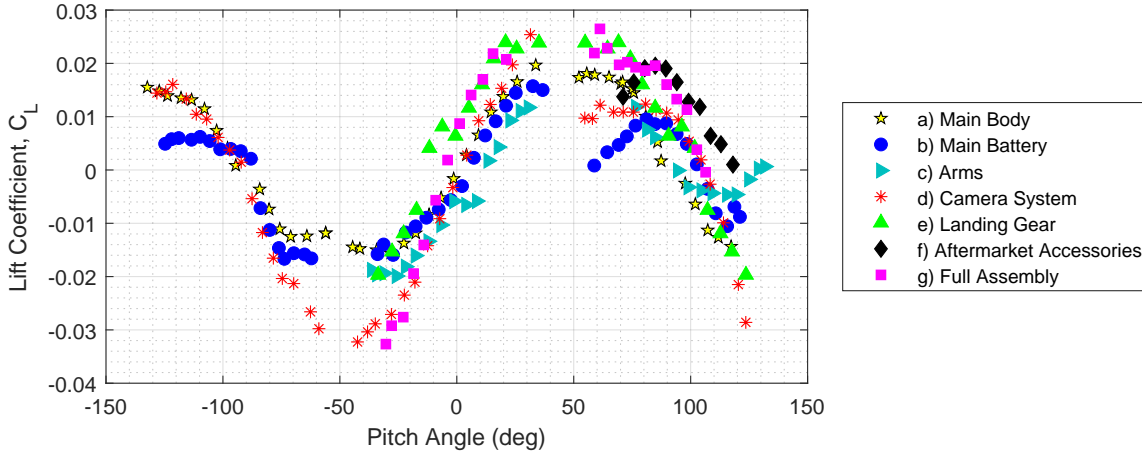
5 Experimental Results

The pitch sweep results and the roll sweep results are presented for each configuration to demonstrate the contributions of the individual components on the overall airframe loads. The results presented are at approximately 15m/s freestream velocity and are non-dimensionalized to a reference area of 1. It should be noted that around that angles around -50° and 50° are missing as the angle adjustments were limited in these areas by either the maximum angle possible with the pitch-wire or, in some configurations, the model itself would approach the wind tunnel walls. In this study, pitch and roll angles are in a typical aircraft reference frame where positive pitch is nose up, and positive roll is right side down. The corrections described in Section 4 have been applied to the presented data, and the different configurations are associated with those presented in 4. The vehicle is mounted at a 90° yaw angle to simulate rolling compared to the pitching mounting.

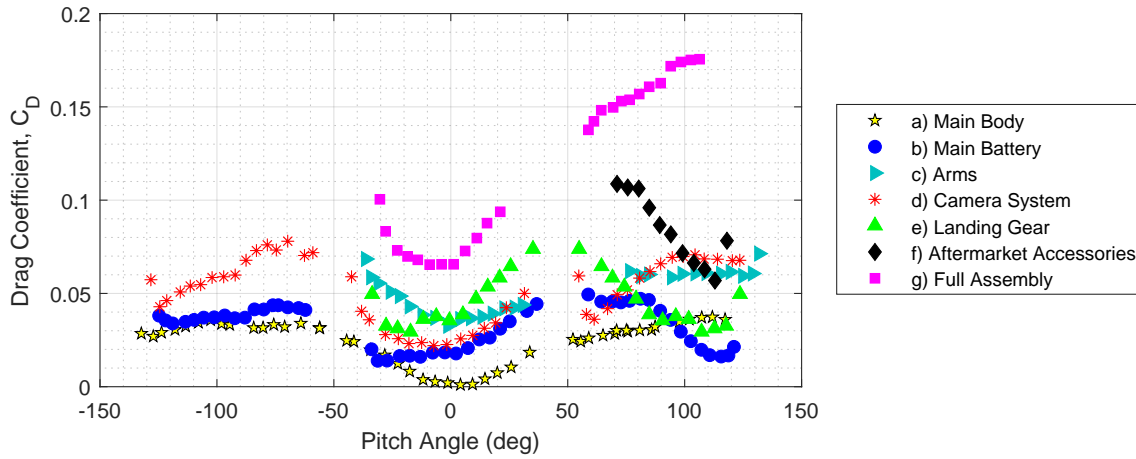
Thus a 0° pitch angle can be related to forward flight with no pitch angle, and a 0° roll angle can be related to flying sideways with no roll angle.

Figure 8 shows the lift and drag coefficients measured at different pitch angles. It should be noted that when the configuration has the landing gear (configurations e, f and g), the pitch angles of -50° or less were not recorded due to mounting conflicts. Figure 8a shows the lift coefficients, which follow a general sinusoidal trend with zero lift near a zero pitch angle. The fully assembled configuration has a maximum lift coefficient of approximately 0.026 and the lift curve slope between -20° to 20° of approximately 0.44 with the presented non-dimensionalization.

Figure 8b shows the measured drag coefficients for each of the configurations. The drag values of the full assembly are approximately a magnitude larger than the previously discussed lift values. As expected, the a and b configurations have the lowest drag. For most configurations, the minimum drag values are near a pitch angle of 0° . All configurations, except for configuration a, are asymmetric, explaining the differences between positive and negative pitch angles. As expected, adding additional components in general increases the overall drag. The landing gear and the aftermarket accessories cause the largest impact on the overall measured drag.



(a) Lift coefficient



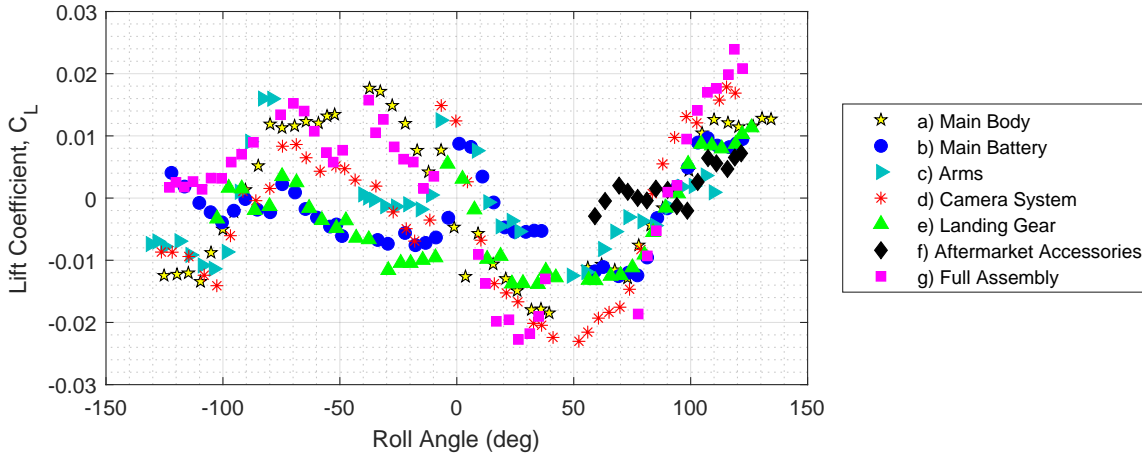
(b) Drag coefficient

Figure 8: Results for all configurations for pitch sweeps at approximately 15m/s.

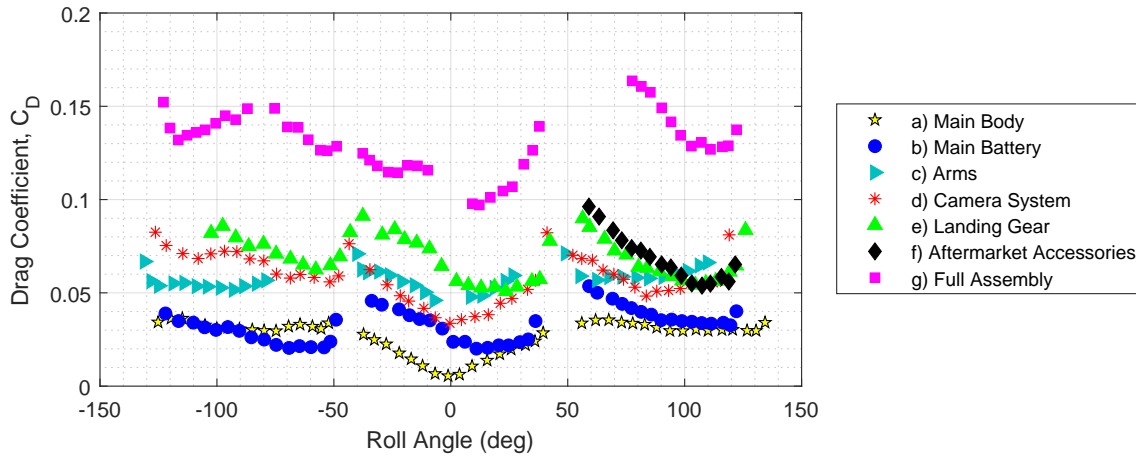
Figure 9 shows the lift and drag coefficients measured at different roll angles. Figure 9a shows the lift coefficient at different roll angles. The lift coefficients of negative roll angles have a less consistent trend between configurations compared to the positive roll angles and the previously discussed pitch angle trends. The maximum lift coefficient of the full assembly is approximately 0.024 (similar to pitch) and lift curve slope between -20° to 20° of approximately 0.037.

Figure 9b shows the drag coefficient at different roll angles. The trends are similar to those presented for different pitch angles, with some notable differences. The negative roll angle for the overall complete assembly has less of a dependence on the roll angle. Similar to the pitch sweep, only configuration a is symmetric, which is evident in the drag results. The landing gear (configuration e) has the most significant impact on the overall drag compared to other components at most roll angles. Additionally, the camera system (configuration d) and the arms (configuration c) have a

similar drag magnitude except for large negative roll angles. Compared to the pitch angles, the aftermarket accessories have less of an additional drag in the roll configurations. On average, the accessories increased the drag by 9% in roll configurations compared to an average of 35% in pitch configurations. With the presented roll and pitch data, there is some scatter, which is expected to be caused by the large amount of turbulent flow caused by such the non-streamlined, bluff bodies.



(a) Lift coefficient



(b) Drag coefficient

Figure 9: Results for all configurations for roll sweeps at approximately 15m/s.

In order to investigate the applicability of using a drag build-up approach to determine the total airframe loads, the drag of each component is isolated. Figure 10 shows a set of curve fits for the rolling drag data previously discussed in Fig. 9b. A high-order sum of sines curve fit was used. In areas where there is no data due to angle limitations, the curve fitting is approximated. The curve fits are subtracted from either configuration a or b to isolate the loads due to each component.

Figure ?? shows the interpolated individual component drag values as well as the sum of the isolated components. The dotted line represented the sum of the isolated components shown in the

same plot without accessories, as the accessories only have data at high roll angles. Comparing the sum of components (dotted line) with the full assembly (solid line) represents a comparison between a load build-up approach and the actual loads. The figure shows that using a load build-up approach for this airframe shows a similar average magnitude, but the trend does not match well (especially at larger roll angles). Some limitations of this drag build-up approach are the approximations made when curve fitting to the wind tunnel data, the interference effects between the airframe components are not accounted for, and there is likely significant turbulent flow separation caused by the bluff bodies, which can result in some variation in the load measurements.

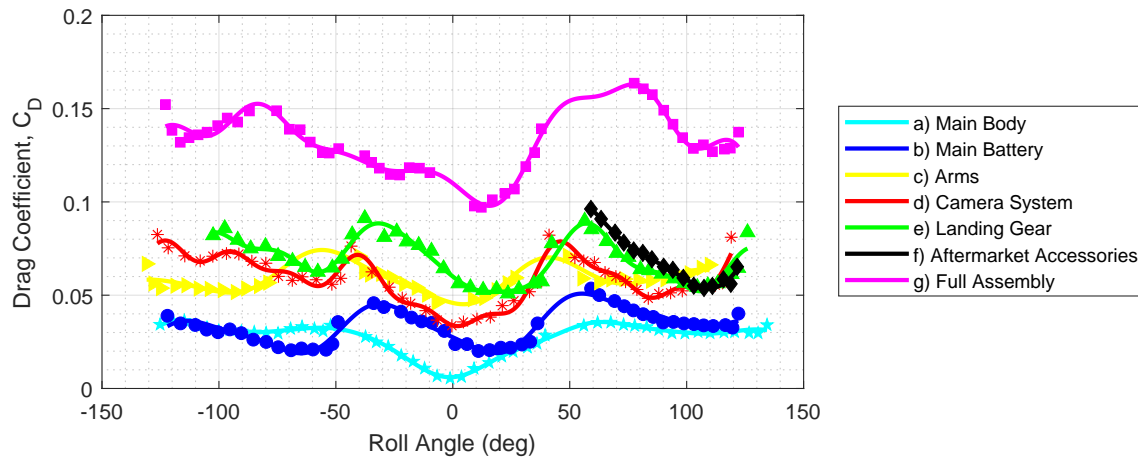


Figure 10: Curve fitting the configuration drag coefficients for the roll cases at 15m/s.

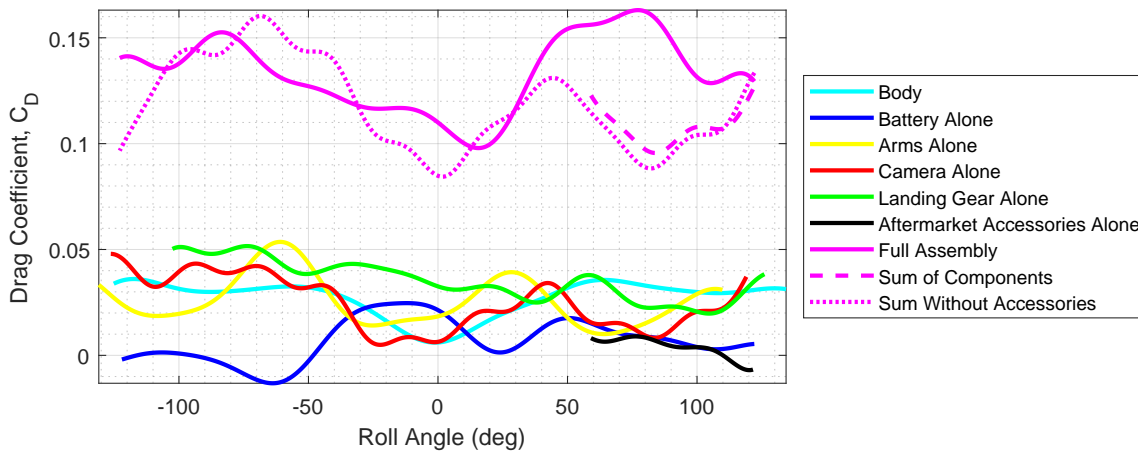


Figure 11: Comparing a load drag-up approach to for the roll cases at 15m/s.

6 Conclusions

A wind tunnel model based on the airframe of the DJI Matrice 210 RTK was created and tested for a better understanding of the airframe loads. Seven configurations were tested with different

components to help quantify the influence of the main airframe components on the total loads. The measured airframe lift and drag values at different roll angles and pitch angles were presented. The following conclusions have been drawn from this study:

- It was shown that the airframe loads have a significant contribution to the overall vehicle loads in forward flight conditions. For the case presented, the airframe loads were over 10% of the overall vehicle loads.
- The three corrections applied to the measured loads included baseload subtraction, blockage effects and buoyancy effects. The base loads had the largest impact on the results, the blockage effects had between 0.56% and 2.9% difference in dynamic pressure, and the buoyancy effects were relatively small with an additional drag that was less than 0.16% of the measured drag values.
- A database was presented for different roll and pitch angles that researchers can use to validate prediction models. The wind tunnel model specifically used components typically used by multirotor UAVs in order to ensure the database is relatable for other vehicles.
- The drag build-up approach with the roll results showed similar overall magnitudes to the fully assembled configuration but did not follow the same trends. With a bluff body that is not streamlined, the measurements have some variations caused by the turbulent nature of these shapes. Additionally, a load build-up approach does not consider the interactional effects between the different components.

7 Acknowledgements

The authors would like to thank Jerry Karpynczyk for their help with setting up the wind tunnel experiment. The authors would also like to thank Dr. Steven Waslander and Ben Isaac for their help with creating the technical drawings and flight test data of the DJI Matrice 210 RTK. This work was made possible through the support of the Ryerson University Aerospace Department.

References

- [1] B. Brandt, J. and S. Selig, M., “Propeller performance data at low reynolds numbers,” in *49th AIAA Aerospace Sciences Meeting*, no. AIAA 2011-1255, Orlando, FL, 2011, AIAA 2011-1255. doi: 10.2514/6.2011-1255
- [2] W. Deters, R., G. Krishnan, and S. Selig, M., “Reynolds number effects on the performance of small-scale propellers,” in *32nd AIAA Applied Aerodynamics Conference*, no. AIAA 2014-2151, Atlanta, GA, 2014, AIAA 2014-2151. doi: 10.2514/6.2014-2151
- [3] A. Kolaei, D. Barcelos, and G. Bramesfeld, “Experimental Analysis of a Small-Scale Rotor at Various Inflow Angles,” *International Journal of Aerospace Engineering*, vol. 2018, Article ID 2560370, 2018.

- [4] B. Theys, G. Dimitriadis, P. Hendrick, and J. De Schutter, “Experimental and numerical study of micro-aerial-vehicle propeller performance in oblique flow,” *Journal of Aircraft*, vol. 54, no. 3, pp. 1076–1084, 2017. doi: 10.2514/1.C033618
- [5] C. Russell, J. Jung, G. Willink, and B. Glasner, “ind tunnel and hover performance test results for multicopter uas vehicles,” in *American Helicopter Society International Annual Forum and Technology Display*, no. 72-2016-374, West Palm Beach, FL, 2016.
- [6] R. Danis, “Investigating forward flight multicopter wind tunnel testing in a 3-by-4 foot wind tunnel,” Master’s thesis, California Polytechnic State University, San Luis Obispo, CA, 2018.
- [7] E. Baris, C. B, and A. G, “Wind tunnel testing of static and dynamic aerodynamic characteristics of a quadcopter,” in *AIAA Aviation 2019 Forum*, no. AIAA 2019-2973, Dallas, TX, 2019, AIAA 2019-2973. doi: 10.2514/6.2019-2973
- [8] S. L. Prudden, A. Fisher, and S. Watkins, “An investigation into the effects rotor wake interference on quadrotor uas forward flight performance,” in *18th Australian Aerospace Congress*, no. ISBN 9781925627213, Melbourne, Australia, 2018.
- [9] T. Carroll, I.-R. E. George, and G. Bramesfeld, “Design Optimization of Small Rotors in Quad-Rotor Configuration,” in *54th AIAA Aerospace Sciences Meeting*. San Diego, CA: AIAA SciTech Forum, 2016, AIAA 2016-1788.
- [10] J. D. Tsaltas and G. Bramesfeld, “Trim routine for multicopter vehicles in straight and level flight,” in *35th AIAA Applied Aerodynamics Conference*, no. AIAA 2017-3054, Denver, CO, 2017, AIAA 2017-3054. doi: 10.2514/6.2017-3054
- [11] B. Barlow, J., H. Rae, W., and A. Pope, *Low-Speed Wind Tunnel Testing*, 3rd ed. New York, United States of America: John Wiley & Sons, 1994.